Final Draft
of the original manuscript:

Peng, Q.; Huang, Y.; Zhou, L.; Hort, N.; Kainer, K.U.:

Preparation and properties of high purity Mg–Y biomaterials

Preparation and properties of high purity Mg-Y biomaterials

Qiuming Peng, Yuanding Huang, Le Zhou, Norbert Hort, Karl Ulrich Kainer

MagIC – Magnesium Innovation Centre, GKSS Forschungszentrum Geesthacht GmbH, Max-Planck-Str. 1, D-21502 Geesthacht, Germany

Abstract

An effective zone solidification method has been found to prepare high purity Mg-Y biomaterials. The corrosion and mechanical properties of the purified middle region are improved remarkably compared with common casting method. The average gain size and secondary dendrite space decrease from the top layer to the bottom layer of the ingot. The oxides, defects and precipitates are mainly enriched in the top layer of the ingot under the impulsion of high thermal gradient. These results are in agreement simulated by finite elemental method using FLOW-3D software. It is confirmed that the mode of scallop symmetric solidification attributes to the purifying process. This zone solidification method not only contributes to high purity Mg-based biomaterials, but also provides a new approach to prepare high performance Mg alloys.

Keywords: Zone solidification; Biomaterials; Purifying; Mg-Y alloy; Properties

---

* Corresponding author. Tel: +49-4152-871932; Fax: +49-4152-871909

E-mail address: qiuming.peng@gkss.de

1 Introduction

Magnesium (Mg) is an exceptionally lightweight material. As one of human metabolism elements, it not only exhibits close mechanical properties to natural bone and outstanding biocompatibility, but also it would be corroded at the pH level (7.4–7.6) and in the high chloride environment of physiological systems [1]. At the same time, the in vivo corrosion of Mg-based implant demonstrated that the formation of a soluble, non-toxic oxide which was harmless for the urine. Moreover, owing to presence in bone tissue, Mg may actually have stimulatory effect on the growth of new bone tissue. These intriguing characteristics have attracted great attention in respect of biodegradable bone implant applications. However, the disadvantage is that the pure Mg would be corroded too fast. Thus, the mechanical integrity is destroyed before the tissue has sufficiently healed. Meanwhile, it would produce a lot of hydrogen gas during the corrosion process [2]. Therefore, the selection of suitable composition of alloys has received much attention. Mg-Ca based, Mg-Al based and Mg-Zn based systems have been considered to implant in human body since the middle of last century [3-6]. However, the rates of the corrosion of these simple alloys were too rapid to allow sufficient time for healing as it is desirable to have the implanted fixture present for at least 12 weeks [7]. Consequently, to improve the corrosion resistance of Mg biomaterial is very important for the industrial application.

As one of active alloying elements, rare earths (RE) could improve the mechanical properties, corrosion properties and creep resistance of Mg alloys. More recently, Witte et.al [8, 9, 10, 11] investigated the in vivo degradation and corrosion properties of LAE442 and WE43. The implanted rods completely depredated in 18 weeks and implants were harvested at 6 and 18 weeks. Furthermore, AZ31, AZ91 and WE43 were found to degrade at similar rates. Heublein et al. [12] had reported that the degradation of AE21 in coronary artery was considered to be linear and drew the conclusion that the vascular implants consisting of Mg alloys seemed to be a realistic alternative

to permanent implants. The previous results provided a direction that the Mg alloys containing RE (non-toxic) is one of potential ideal biomaterials.

However, RE is very liable to react with the impurity elements such as H, O, F, Cl, Fe and Cu [13]. When RE is added into Mg alloys, the precipitates containing RE and impurity elements could form. The existences of these impurities definitely not only decrease the content of RE, but also affect the mechanical integrity of components and their corrosion properties. More importantly, the existence of some impurities absolutely brings some harmful effects to human body when Mg-RE alloys are used as an implant. Consequently, investigations on the preparation of high purity Mg-RE alloys are very interesting and necessary for either scientific researches or practical applications.

In present work, the high purity Mg-8Y alloy was prepared by zone solidification method. The microstructure and distribution of impurities in ingots were investigated. The influence of different distribution of impurities on the corrosion and mechanical properties was also studied. Furthermore, the purifying mechanism was explored by the simulation of finite elemental method using FLOW-3D software.

2. Experimental procedures

2.1 Preparation process

The zone solidification was characterized with the ingots gradually cooled by water. Its detailed description is as follows. The Mg-8Y alloy was prepared by pure Mg and Y in a steel crucible under a cover gas mixture of CO_2 and SF_6. After mixing at 730 °C for 1.5 h, the alloy was cast to the mould preheated at 500 °C. The filled mould was held at 670 °C for 1 h under the protective gas. Then, the whole steel crucible with the melt was immerged into the continuous cooling water at 10 mm/s. When the bottom of steel crucible touched the water, it stopped for 1 second. As soon as the liquid level of inside melt is alignment with the height of outside water, the solidification process was finished. The size of ingot (purified state) is 6 cm × 12 cm × 20 cm. The common casting was also carried out for comparison with zone solidification method. The melt was kept at 700 °C for 20

minutes and then was directly cast into mould with the same size without water cooling (common state).

2.2 Corrosion properties

Potentiodynamic polarisation tests were carried out to evaluate the corrosion rate of samples using a potentiostat system. A typical three electrode cell, with the encapsulated sample by epoxy resin as a working electrode (50 mm^2 exposed area), a saturated Ag/AgCl electrode as reference electrode, and a platinum mesh as counter electrode were used in the tests. All polarisation tests were conducted in 3.5 wt. % NaCl solutions at a scan rate of 0.5 mVs^{-1} after exposure period of 10 minutes.

2.3 Microstructure characterization

Microstructural investigations were performed using polarization microscopy (PM) and scanning electron microscopy (SEM) equipped with energy dispersive X-ray analysis (EDX). The content of impurities was measured by X-ray fluorescence spectroscopy (XFS). For PM and EDX analysis, the standard procedures including grinding, polishing and etching were applied. The samples for PM were etched in an acetic picral solution to reveal grain boundaries. The grain size was measured using the linear intercept method.

2.4 Mechanical properties

The hardness was carried out by Vickers hardness, the test load and the dwell time were 100 g and 15 s, respectively. The compression tests were performed using standard mechanical testing machine at both room temperature and elevated temperatures with a strain rate of 1.7×10^{-3} s^{-1}. The samples were soaked at the test temperatures for 20 minutes in order for the homogenous distribution of temperature before compressive tests.

2.5 Solidification simulation

The solidification process such as the change of temperature with solidification time was simulated by finite elemental method using FLOW-3D software. Considering on the similarity between Mg-8Y alloy and WE43 alloys, the input parameters such as specific heat and thermal conductivity were cited from the results of WE43 [14]. The temperatures of solidus and liquidus were directly taken from the binary Mg-Y phase diagram. The detailed thermal parameters of the specimen are listed in Table 1.

3. Results and discussion

3.1 Corrosion properties and content of impurities

The polarization curves of different parts are shown in Fig. 1. The bottom layer exhibited highest potential. On the contrary, the cleared middle region showed lowest one. The polarization curves were used to estimate the corrosion current density, i_{corr}, at E_{corr}, by Tafel extrapolation of the cathodic branch. The corrosion current density, i_{corr} (mAcm^{-2}), can be related to the corrosion rate, P_i (mmy^{-1}), using the following conversion equation [15].

$$P_i = 22.85 i_{corr} \tag{1}$$

According the above conversion equation, the corrosion rates of different portions are obtained. The detailed corrosion results of the purified state and common state are presented in Fig. 2. The average corrosion rate of common as-cast state is about 7.11 mmy^{-1}. However, the average corrosion rate of the purified alloy in the middle region is about 2.17 mmy^{-1}, which is only about 30 % of that of common state specimen. The distributions of impurities (Fe, Cu and Ni) in the different areas of the alloys are also shown in Fig. 2. For the sample prepared by zone solidification, the amount of the impurities in the top layer or the bottom layer of the ingot is higher than that in the middle region. The content of impurities in the middle region of ingot prepared by zone solidification is lower compared with the alloy prepared by common casting. This indicates that the

zone solidification can prepare the high purity Mg alloys by separating the impurities into both the top and bottom layers of the ingots, which beneficially reduce the opportunity to bring the harmful impurities into the human body when the Mg alloys are used as degradable biomaterials.

This trend of impurities content is mainly related to the above results of potentials. Due to the low hydrogen overvoltage, the existence of Fe impurity provides active cathodic sites compared to the Mg matrix, and causes severe micro-galvanic corrosion [16]. The higher content of Fe in impurities, the more efficient cathodes constitute. Thus, it leads to the high current density and corrosion rate. On the other hand, the existence of Fe impurity forms the type of microcellular sub-structure. It not only accelerates the dot corrosion on the surface, but also readily breaks the anti-oxide membrane during the oxidized process owing to the dissolution of Fe. As a result, the fresh surface of matrix is always exposed to liquid. The similar effect of Fe melted in an iron crucible on pure Mg was investigated by Rutter and Chalmers [17]

3.2 Microstructures

The typical PM micrographs of the purified state Mg-8Y alloy taken from the horizontal-section and vertical-section are shown in Fig. 3. The results exhibit no macroscopic defect on the surface of the sample. The alloy is mostly composed of equiaxed grains. Inside the grains, the secondary dendrites are also observed. Some eutectic phases formed during the solidification distribute along the grain boundaries. There are two zones of defects or impurities locating near the top and the bottom of the ingot. The width of defect band in the top layer is around 400-600 μm. The thickness of the impurity band in the bottom layer is larger than that in the top layer. It was observed that the majority of the impurities segregated at the bottom. Along the vertical direction, the grains exhibit obvious preferential growth from the bottom to the top. Microstructures in the middle region prepared by common casting are also shown in Fig. 3. Some dot-like impurities are observed in the matrix. The average grain size (AGS) and average secondary dendrite spacing (ASDS) are 950 μm and 42 μm, respectively.

The changes of AGS and ASDS as a function of the position (distance starting from the top of the cleaned sample) are depicted in Fig. 4. In the middle region, the AGS remains a relatively stable plateau. The AGS of the middle region of purified state is 500 μm. The ASDS is around 32 μm. Both AGS and ASDS decrease obviously in the bottom. Compared with the common casting, the purifying process can not only decrease the AGS but also highly affect the ASDS during the solidification.

Compared with the specimen prepared by common casting, the AGS of purified alloy is greatly dependent on the position. Namely, the AGS keeps relatively unanimous in the middle region, but it changes obviously in the bottom layer. There are two main reasons accounting for this result. Firstly, the structure size is dependent on the atomic diffusion ability during solidification. Meanwhile, the rate of atomic diffusion is strongly related to the temperature [18, 19]. In the present alloy, the different grain size in the different portions mainly attributes to the different temperature gradient ($\underline{\Delta T} = dT/dx$) that the temperature difference between the liquid metal and the water. Similar suggestion was described by Shewmons that an effective force exerted by the temperature gradient, which leads to thermal segregation of the two components [20]. When the bottom of the crucible touched the cooling water, the liquid in the bottom solidified immediately under the control of the high $\underline{\Delta T}$. At the same time, the outside temperature of crucible is a constant and the $\underline{\Delta T}$ decreases along the centre axis from the bottom to the top. Thus, the grain size increases with the specimen falling into the water. Secondly, since the solidification time is short, the final microstructure is directly associated with the amount of nucleates. This high undercooling has a remarkable effect on nucleation rate and the growth rate of the dendrites. During the first stage of solidification, it is essentially nucleation-controlled. Taking account of the short time of solidification process, the final microstructure is mainly associated with the amount of nucleants. The particles, formed by the Y element and the other impurities such as Fe, Cu or Ni sedimentated owing to their high densities, could act as the nuclei during the solidification. The nuclei formed on the surface of these particles require a low thermal super-cooling to surpass the high barrier of

initial nucleation. Eventually, the fine microstructure is observed at the bottom layer. Lee [21] reported the additions of Zr, Si, and Ca to pure Mg resulted in efficient grain refinement by changing their growth restriction or as secondary phase particles.

3.3 Distribution of precipitates

Fig. 5 shows the SEM micrographs of the purified state alloy in the different portions. In the top layer, the porosities and some precipitates (A, B and C) are observed along the dendrite boundaries. The chemical compositions of these precipitates were determined by EDX. The detailed contents of elements are listed in Table 2. The coarse dot-shape precipitate A is mainly composed of Y, O and a little S; the blocky precipitate (B) consists of Fe, Cu, Ni and Y; and the fine dot-shape phase C mainly contains Mg, O and a little F. In centre region, the discontinuous precipitate (D) distributing along the dendritic boundaries mainly contains Mg and Y, which can be identified as $Mg_{24}Y_5$ eutectic phase. There is a separated band with the distribution of impurities observed near the bottom. The left side is the clear zone. Some irregular precipitates (E) are observed on the right side. According to the EDX results, the precipitates are mainly enriched with Y, Fe, Cu and Ni elements. It can be inferred that these impurities have been sedimentated during the purifying process by the chemical reactions. Their distribution and morphologies were kept intact owing to the high cooling rate in this region.

3.4 Mechanical properties

The relationship between hardness and section position is shown in Fig. 6. The similar trends along both vertical direction and horizon direction are observed. Namely, the hardness decreased slightly from the top to the middle, and it kept stable during the middle region, then, it increased near to the bottom. However, the standard deviation changed greatly from the top to the bottom. The higher values were obtained in the top and bottom layers. It implied the hardness was non-

homogonous in these areas compared with the middle region. It is mainly related to the segregation of large size precipitates and defects (observed in 3.1 section).

The compressive properties including ultimate compressive strength (UCS), yield strength (YS) and elongation (ε) ?of the specimens from room temperature to 250 °C are listed in Table 3. It can be seen that the purified sample exhibits higher mechanical properties during the investigated temperature range. The UCS and YS decrease with the increase of temperatures, monotonically. The maximum values of UCS, YS and ε are 257 MPa, 156 MPa, and 14 % at room temperature, respectively. The mechanical properties of the samples keep high value even the temperature is increased to 150 °C. Compared to the purified state samples, the common state ones exhibit lower mechanical strengthen and weaker ductility at room temperature. The decreased mechanical properties are mainly associated with the coarsened grain and the existence of the impurities in the matrix.

3.5 Purifying mechanism

The solidification process of zone solidification was simulated by FLOW-3D software. The model is used to determine temperature profiles and the movement of solidification fronts. Fig. 7 shows the temperature contours at different instants of time during the solidification. As seen from the results, the temperature profile in the bottom is almost scallop symmetric at the beginning of the solidification. The existence of temperature gradient $\underline{\Delta T}$ accounted for the solidification turns, namely, at the same level plane, the temperature at the centre is lower than that of the edge. When the bottom touched the water surface and stopped for 1 second, the bottom part solidified immediately with the high super-cooling. Thus, the impurities kept the same distribution in the melt (as shown in Fig. 5). As the solidification proceeds, the scallop curves of temperature extended from the bottom to the surface. The impurities were pushed and concentrated along the solid/liquid interface. Finally, the matrix and the impurities were separated completely.

Previous investigations [22, 23] indicated that the defect zones or slag entrapments were observed in the alloys prepared by common casting processes. The content of alloying elements changed largely along the transversal direction. The AGS and ASDS near to the edge were smaller than the centre. These distinctness's mainly lie in the different solidifying turns. For previous common cast, the liquid near to the edge firstly solidified at the beginning of solidification. Thus, the map of temperature was expressed as following: the edge temperature is lower than the centre. As a result, the impurities would segregate in the centre zone. Therefore, the defect zone/skin region was formed in the common casting samples [24]. In contrast, at the beginning of zone solidification, the temperature profile of zone solidification was scallop symmetric. The centre would solidify firstly at the same lever of latitude. The map of temperature was formed as following: the edge temperature is higher than the centre. Thus, the impurities would enrich on the surface of the specimen during the solidification. Consequently, the middle part would be purified well.

4. Conclusions

In summary, the zone solidification is an effective way to prepare high purity Mg-Y based biomaterials. Compared with common methods, this approach exhibits following advantages: (i) purifying alloys and improving the corrosion resistance and mechanical properties of the matrix; (ii) decreasing the grain size and secondary dendrite space; (iii) simple and controlling process. The improvement of these properties is mainly related to the decrease of impurities during the zone solidification process. The impurities are segregated in surface or bottom layers owing to the high temperature gradient and scallop solidification turns.

Acknowledgements

References

[1] Staigera MP, Pietaka AM, Huadmaia J, Dias G. Magnesium and its alloys as orthopedic biomaterials: a review. Biomaterials 2006;27:1728-1734.

[2] Zreiqat H, Howlett CR, Zannettino A, Evans P, Schulze-Tanzil G, Knabe C, et al. Mechanisms of magnesium-stimulated adhesion of osteoblastic cells to commonly used orthopaedic implants. J Biomed Mater Res 2002;62:175-184.

[3] Troitskii VV, Tsitrin DN. The resorbing metallic alloy 'Osteosinthezit'as material for fastening broken bone. Khirurgiia 1944;8:41-44.

[4] Li ZJ, Gu XN, Lou SQ, Zheng YF. The development of binary Mg–Ca alloys for use as biodegradable materials within bone. Biomaterials 2008;29:1329-1344.

[5] McBride ED. Absorbable metal in bone surgery. J Am Med Assoc 1938;111:2464-2467.

[6] Zhang SX, Zhang XN, Zhao CL, Li JA, Song Y, Xie C, et al. Research on an Mg–Zn alloy as a degradable biomaterial. Acta Biomaterialia, doi:10.1016/j.actbio.2009.06.028.

[7] Witte F, Hort N, Vogt C, Cohen S, Kainer KU, Willumeit R, et al. Degradable biomaterials based on magnesium corrosion. Current Opinion in Solid State and Materials Science 2008;12:63-72.

[8] Witte F, Kaese V, Haferkamp H, Switzer E, Meyer-Lindenberg A, Wirth CJ, et al. In vivo corrosion of four magnesium alloys and the associated bone response. Biomaterials 2005;26:3557-3563.

[9] Witte F, Fischer J, Nellesen J, Beckmann F. Microtomography of magnesium implants in bone and their degradation. In: Progress in biomedical optics and imaging – proceedings of SPIE 2006, San Diego, CA; 2006.

[10] Witte F, Fischer J, Nellesen J, Crostack HA, Kaese V, Pisch A, et al. In vitro and in vivo corrosion measurements of magnesium alloys. Biomaterials 2006;27:1013-1018.

[11] Quach NC, Uggowitzer PJ, Schmutz P. Corrosion behaviour of an Mg-Y-RE alloy used in biomedical applications studied by electrochemical techniques. Comptes Rendus Chimie 2008;11:1043-1047.

[12] Heublein B, Rohde R, Kaese V, Niemeyer M, Hartung W, Haverich A. Biocorrosion of magnesium alloys: a new principle in cardiovascular implant technology?. Heart 2003;89:651-656.

[13] Emley EF. Principles of Magnesium Technology. Pergamon press 1966:157-187.

[14] Bruce WE, Baxter EF. Diffusion in solid-Earth systems. Earth Planetary Sci Lett. 2007;253:307-327.

[15] Zhao MC, Liu M, Song GL, Atrens A. Influence of pH and chloride ion concentration on the corrosion of Mg alloy ZE41. Corr Sci 2008;50:3168-3178.

[16] Song GL, Asterns A. Corrosion Mechanisms of Magnesium Alloys. Adv Eng Mater 1999;1:11-13.

[17] Rutter JW, Chalmers B. A prismatic substructure formed during solidification metals. Canada J Phys 1953;31:15-39.

[18] Garcia AL, Tikare V, Holm EA. Three-dimensional simulation of grain growth in a thermal gradient with non-uniform grain boundary mobility. Scripta Mater 2008;59:661-664.

[19] Shewmon P. Diffusion in metals. Ind Eng Chem 1959;51:402-405.

[20] Lee YC, Dahle AK, StJohn DH. The Role of Solute in Grain Refinement of Magnesium. Metall Mater Trans A 2008;31:2895-2905.

[21] MEL. Magnesium Elektron Datasheet 467: Elektron WE43; 2005.

[22] Weile JP, Wood JT, Klassen RJ, Berkmortel R, Wang G. Variability of skin thickness in an AM60B magnesium alloy die-casting. Mater Sci Eng A 2006;419:297-305.

[23] Chakrabarti AK. Casting defects and defect diagnosis by NDT. Casting Technology and Cast Alloys. Prentice Hall of India. 2007;P:235-254.

[24] Peng QM, Wang LD, Wu YM, Wang LM. Microstructure and strengthening mechanism of die-cast Mg-Gd based alloys. J Mater Res 2008;23:1269-1275.

Table captions

Table 1 Thermophysical parameters of simulated process

Table 2 The detailed element content of main precipitates in the different zone (wt.%)

Table 3 The compression properties of Mg-8Y alloy at different temperatures (standard deviation is given in parenthesis).

Table 1 Thermophysical parameters of simulated process

Thermo physical parameters	Mg-8Y alloy
Thermal conductivity ($Wm^{-1} K^{-1}$)	51.3
Specific heat ($Jkg^{-1}K^{-1}$)	966
Density (kgm^{-3})	1853
Liquidus temperature ($^{\circ}C$)	645
Solidus temperature ($^{\circ}C$)	593

Table 2. The detailed element content of main precipitates in the different zone (wt.%)

Elements	A	B	C	D	E
Mg			12.24	62.55	18,18
Y	84.41	88.24	73.77	29.45	81.05
O	13.68	10.32	11.35		
S	1.91				
F			2.64		
Fe		0.84			1.12
Cu		0.42			0.27
Ni		0.18			0.28

Table 3. The compression properties of Mg-8Y alloy at different temperatures (standard deviation is given in parenthesis).

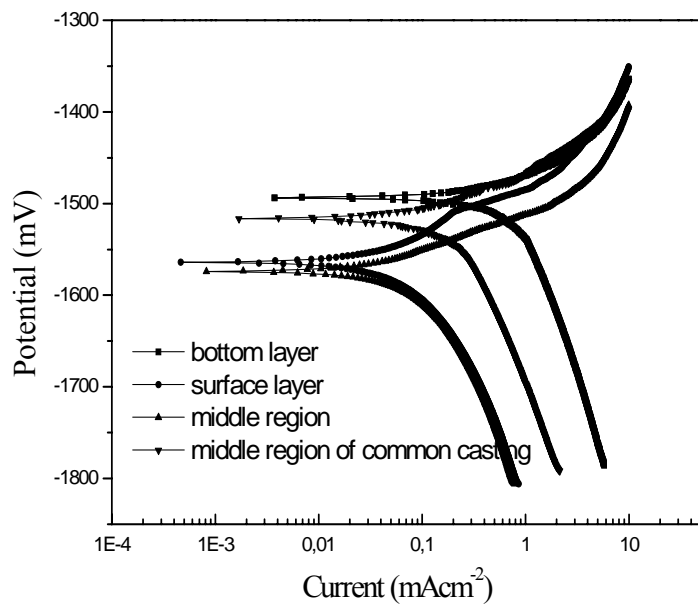| Temperature °C	Middle part of purified state sample			Middle part of common state sample		
	UCS (MPa)	YS (MPa)	ε (%)	UCS (MPa)	YS (MPa)	ε (%)
25	257 (5)	156 (4)	14 (3)	201 (12)	102 (7)	10 (4)
150	228 (6)	121 (5)	17 (3)	183 (14)	86 (8)	14 (3)
250	203 (7)	90 (4)	21 (2)	156 (15)	58 (8)	20 (4)

Figure captions

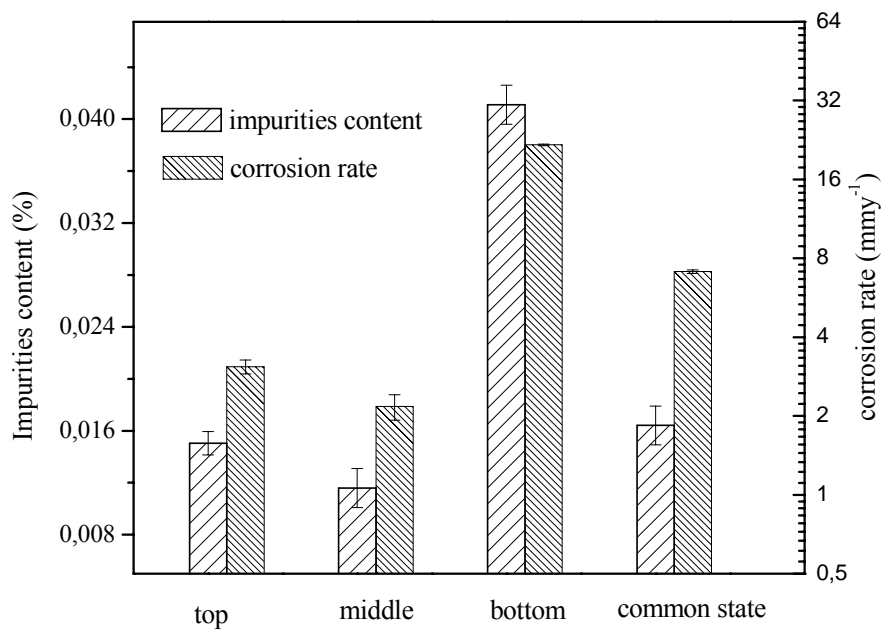Fig. 1 The polarisation curves of different sections of the Mg-8Y alloy.

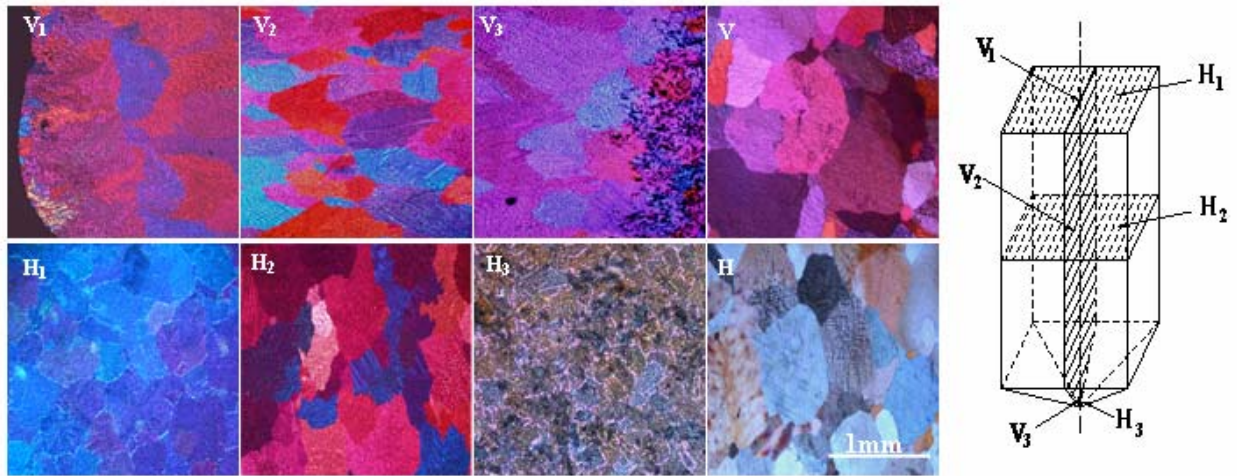Fig. 2 The impurities (Fe, Cu and Ni) contents and corrosion rates of the Mg-8Y alloys in the different sections

Fig. 3 V-1 to V-3 are the structures of vertical-section direction of the purified state ingots; H-1 to H-3 are the structures of horizontal-section direction of the purified state ingots; V and H are the vertical and horizontal sections in the middle region of the common state ingots.
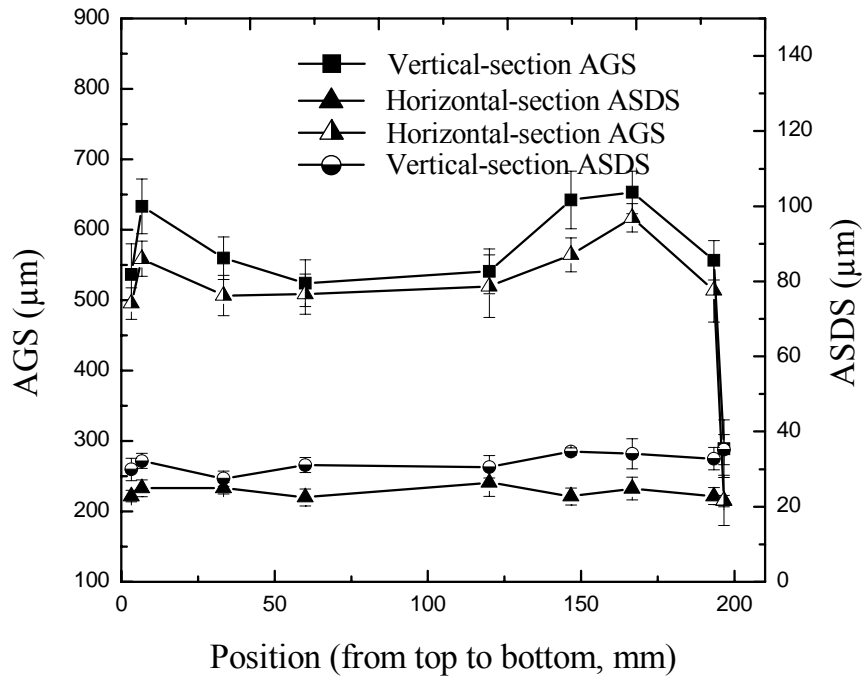
Fig. 4 The horizontal-section AGS/ASDS and vertical-section AGS/ASDS change depending on the sections.

Fig. 5 The typical SEM graphs of the different sections of purified state Mg-8Y alloy.

Fig. 6 The hardness of different portions of purified state specimen.

Fig. 7 FLOW-3D simulated solidification process of Mg-Y alloy at different time steps: a = 1s; b = 3s; c = 8s; d = 12s.

Fig. 1. The polarisation curves of different sections of the Mg-8Y alloy.

Fig. 2. The impurities (Fe, Cu and Ni) contents and corrosion rates of the Mg-8Y alloys in the different sections

Fig. 3. V-1 to V-3 are the structures of vertical-section direction of the purified state ingots; H-1 to H-3 are the structures of horizontal-section direction of the purified state ingots; V and H are the vertical and horizontal sections in the middle region of the common state ingots.

Fig. 4. The horizontal-section AGS/ASDS and vertical-section AGS/ASDS change depending on the sections.
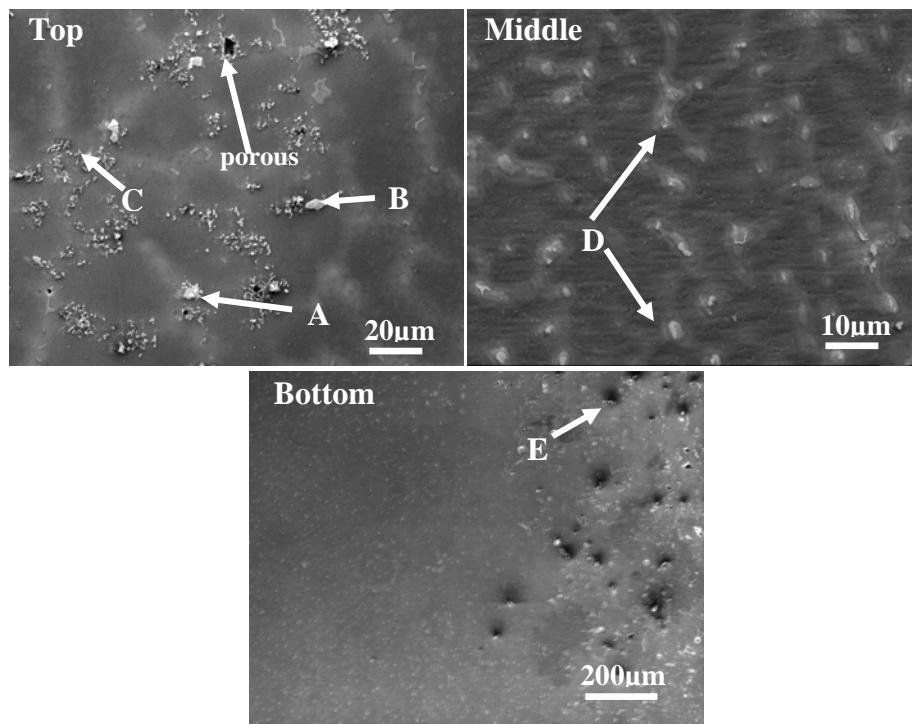
Fig. 5. The typical SEM graphs of the different sections of purified state Mg-8Y alloy.
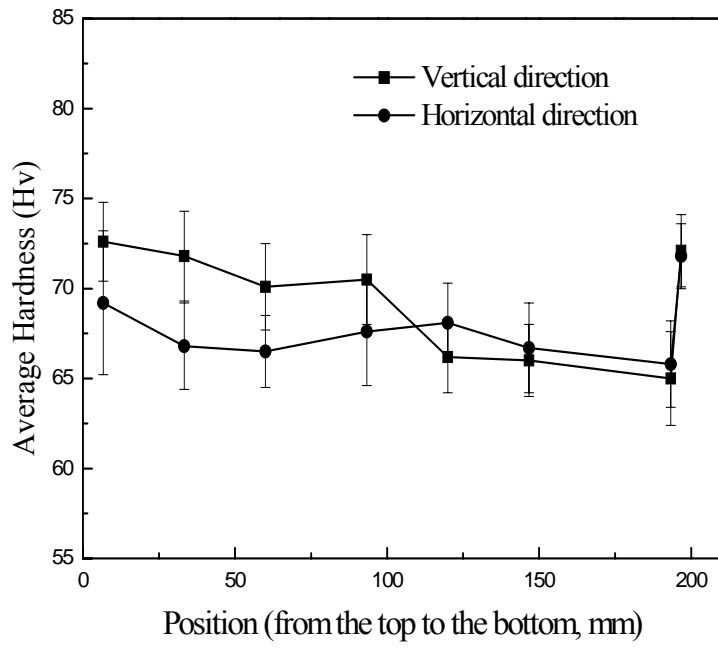
Fig. 6. The hardness of different portions of purified state specimen.
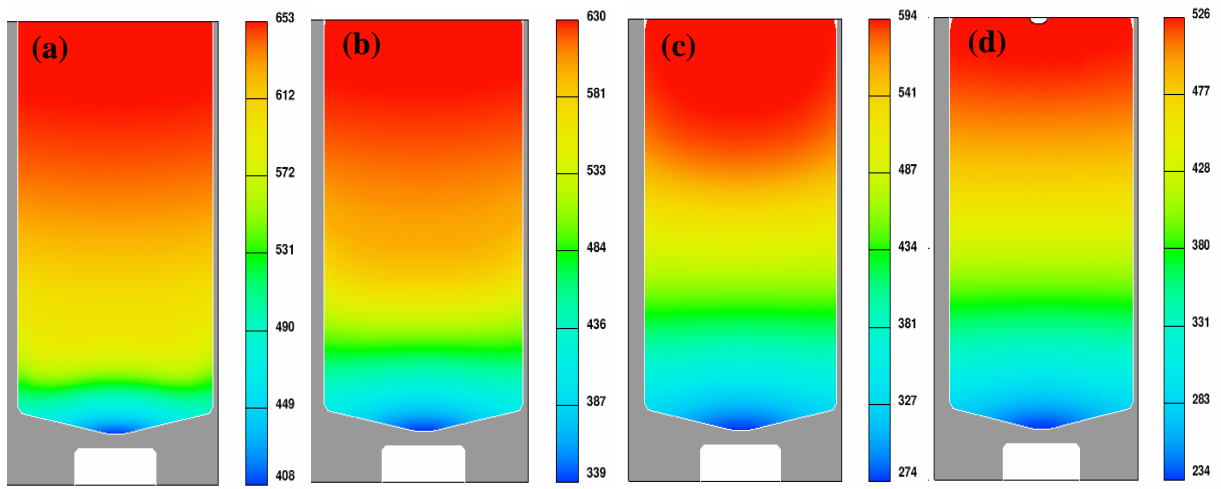
Fig. 7. FLOW-3D simulated solidification process of Mg-8Y alloy at different time steps: a = 1s; b = 3s; c = 8s; d = 12s.